Journal of
Materials Chemistry C

PAPER

View Article Online
View Journal | View Issue

Cite this: *J. Mater. Chem. C*, 2023, **11**, 4846

A double heterohelicene composed of two benzo[*b*]phenothiazine exhibiting intense room-temperature circularly polarized phosphorescence†

Shunya Tanaka,[a] Daisuke Sakamaki,*[a] Naoki Haruta,[bcd] Tohru Sato,[bcd] Masayuki Gon,[e] Kazuo Tanaka[e] and Hideki Fujiwara*[a]

In this work, we report a novel double N,S-hetero[5]helicene composed of two benzo[*b*]phenothiazines (**2**) that exhibits long-lived circularly polarized room-temperature phosphorescence (RTP). Compared with the previously reported *N*,*O*-analogue composed of two benzo[*b*]phenoxazines (**1**), **2** emitted more intense phosphorescence with a longer lifetime than **1** in a frozen solution at near liquid nitrogen temperature and even at room temperature when doped in a β-estradiol matrix. The intense and long-lived phosphorescence of **2** was fully explained by theoretical calculations. The optical resolution of **2** was successfully achieved, and the chiroptical properties of **2** were investigated. We found that **2** doped in a matrix exhibits strong dual circularly polarized luminescence originating from fluorescence ($|g_{\mathrm{CPL}}| = 1.7 \times 10^{-2}$) and long-lived phosphorescence ($|g_{\mathrm{CPL}}| = 5 \times 10^{-3}$, lifetime of 0.16 s, and Φ_{p} of 30%) at room temperature. **2** is a very rare example of a purely-organic helicene that exhibits long-lived circularly polarized RTP from a non-aggregated state.

Received 10th March 2023,
Accepted 20th March 2023

DOI: 10.1039/d3tc00871a

rsc.li/materials-c

Introduction

In the development of functional π-conjugated materials, the introduction of heteroatoms into the molecular skeleton is a useful strategy for controlling physical properties. In this context, heteroacenes, in which some carbon atoms of acenes are replaced by heteroatoms, are one of the key components of functional π-conjugated materials.[1] Heteroacenes bearing amino nitrogen atoms in the molecular skeleton, such as phenoxazine, phenothiazine,[2] and hydroazaacenes,[3,4] are useful compounds that exhibit multiple functions, such as electron-donating ability, photophysical properties, and charge transport properties. In 2015, we established a simple method for the synthesis of double heterohelicenes by tandem oxidative coupling of heteroacenes with an NH group.[5–8] Heterohelicenes have attracted recent interest as potential materials with unique optical and electronic properties derived from chirality, such as chiroptical properties represented by circular dichroism (CD) and circularly polarized luminescence (CPL).[9–16] We have recently succeeded in synthesizing a double *N*,*O*-hetero[5]helicene **1** (Fig. 1) composed of two benzo[*b*]phenoxazines (**BPO**),[7] and we comprehensively compared **1** and a double *N*,*O*-hetero[5]helicene composed of dibenzo[*b*,*i*]phenoxazines[5] to clarify how the presence or absence of

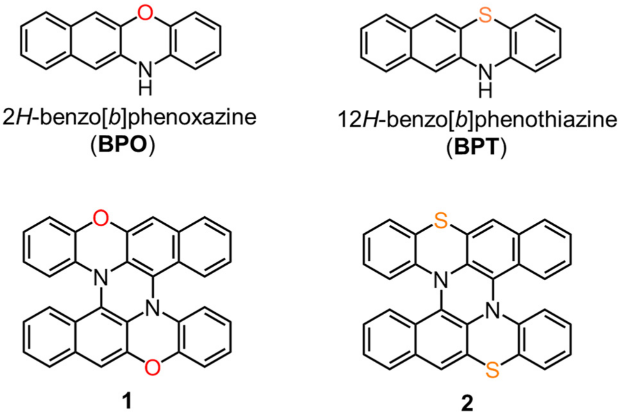

Fig. 1 Structures of double heterohelicenes **1**, **2** and their monomer units.

---

[a] Department of Chemistry, Graduate School of Science, Osaka Metropolitan University, Naka-ku, Sakai-shi, Osaka 599-8531, Japan. E-mail: sakamaki@omu.ac.jp, hfuji@omu.ac.jp

[b] Fukui Institute for Fundamental Chemistry, Kyoto University, Sakyo-ku, Kyoto 606-8103, Japan

[c] Department of Molecular Engineering, Graduate School of Engineering, Kyoto University, Nishikyo-ku, Kyoto 615-8510, Japan

[d] Unit of Elements Strategy Initiative for Catalysts & Batteries, Kyoto University, Nishikyo-ku, Kyoto 615-8510, Japan

[e] Department of Polymer Chemistry, Graduate School of Engineering, Kyoto University, Nishikyo-ku, Kyoto 615-8510, Japan

† Electronic supplementary information (ESI) available. CCDC 2103647. For ESI and crystallographic data in CIF or other electronic format see DOI: https://doi.org/10.1039/d3tc00871a

additional benzo moieties affects their structures and properties. In the work, we found an unexpected result that the additional benzo moieties invert the CPL signs of the double helicenes of the same helicity. The previous work demonstrated that the small structural changes in this class of helicenes could result in significant differences in electronic properties. Following the work, we herein focus on the effects of replacing the heteroatoms of **1**. We synthesized a novel double N,S-hetero[5]helicene **2** (Fig. 1) composed of two benzo[*b*]phenothiazines (**BPT**), which is a sulfur analogue of **1**. By comparing **1** and **2**, we found that replacing oxygen with sulfur significantly changes the emission properties of this type of double helicenes. Interestingly, enantiopure **2** doped in a matrix emits dual CPL at room temperature originating from fluorescence and long-lived room-temperature phosphorescence (RTP).[17–26]

Results and discussion

The double N,S-hetero[5]helicene **2** was synthesized by the tandem oxidative coupling of **BPT** (Scheme S1, ESI†). **BPT** was easily prepared by solvent-free condensation of *o*-aminothiophenol and 2,3-dihydroxynaphthalene on a multigram scale. The oxidation of **BPT** with 0.5 equiv. of DDQ gave a cruciform dimer (**3**) in 60% yield. Further oxidation of the dimer **3** with DDQ in the presence of $Sc(OTf)_3$ resulted in intramolecular C–N bond formation and gave **2** in a 60% yield. **2** was also obtained by one-pot tandem oxidation of **BPT** without isolating **3** in 34% yield.

Rac-**2** crystallized in tetragonal space group $I4_1/a$, and all the molecules in the crystal are crystallographically equivalent. The structure of (*M*,*M*)-enantiomer of **2** is shown in Fig. 2a. **2** possesses a C_2 symmetric structure due to the existence of a 2-fold axis penetrating the central 6-membered ring. The benzene moieties stand up steeply by bending the N,S-containing 6-membered rings along the N–S axis. Consequently, **2** is highly asymmetric for the C_2 axis; the upper face is a convex side with the two benzene rings projecting upward, and the other face is an almost planar concave side. The torsion angle around the helicene moieties of **2** (60.7°) was much larger than that of **1** (48.3°),[7] indicating that the replacement of oxygen with sulfur atoms increased the torsion angle. The sum of the angles around the nitrogen atoms of **2** decreased to 350.6° compared to that of **1** (avg. 357.6°), reflecting the decrease in planarity around the nitrogen atoms. The packing structure of **2** was significantly different from **1**. In the crystal of *rac*-**1**, each enantiomer was aligned in columnar stacks. On the other hand, in the crystal of *rac*-**2**, opposite enantiomers are stacked alternately by facing the same faces (concave-concave and convex-convex) (Fig. 2b).

The DFT structural optimization of **2** converged to the C_2 symmetric structure in accord with the crystal structure. The shapes of the frontier Kohn–Sham MOs of **1** and **2** are basically the same (Fig. 3). The MO coefficients on the chalcogen atoms are scarce for HOMO and LUMO but more significant for HOMO−1 and HOMO−2 in both **1** of **2**. The HOMO of **2** (−5.04 eV) is lower than that of **1** (−4.80 eV) by 0.24 eV, reflecting the low-lying HOMO level of **BPT** (−5.30 eV) compared with that of **BPO** (−5.07 eV) (Fig. S21, ESI†). Electrochemical measurements confirmed that the first oxidation potential of **2** (0.25 V *vs.* ferrocene/ferrocenium) was higher than that of **1** by 0.20 V (Fig. S5 and Table S2, ESI†). The LUMO level of **2** (−1.63 eV) is almost the same as that of **1** (−1.62 eV). The oscillator strength (*f*) of the HOMO–LUMO transition is predicted to be very small ($f = 0.0014$), similar to that of **1** ($f = 0.0002$) (Fig. S22, ESI†). This is because the HOMO and LUMO of **1** and **2** belong to the same irreducible representation (*a*). In **1** and **2**, π-conjugation is mainly elongated in the direction perpendicular to the C_2 axis, but the electronic transitions perpendicular to the C_2 axis are symmetry forbidden for the HOMO–LUMO transition in this case.

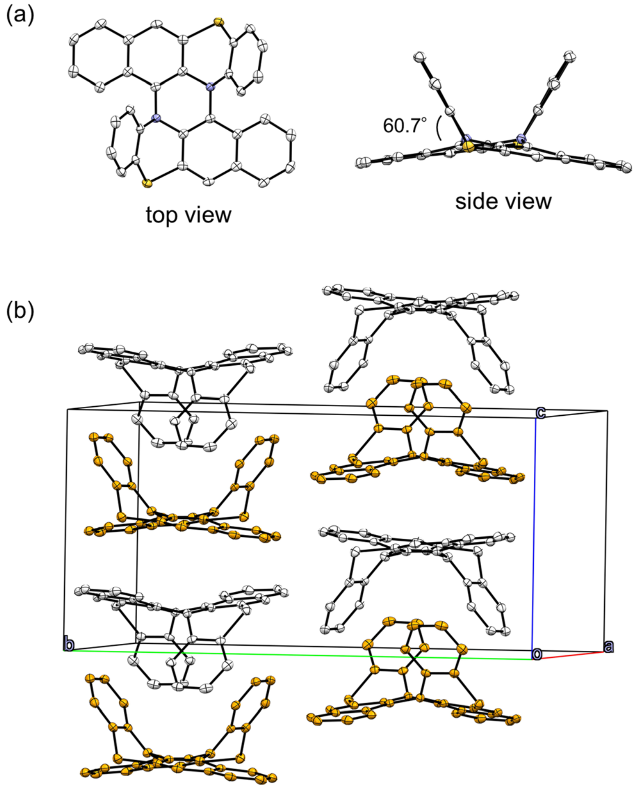

Fig. 2 (a) ORTEP drawing of (*M*,*M*)-**2** in the racemic crystal and (b) crystal packing structure of *rac*-**2**. Thermal ellipsoids are set at 50% probability. Hydrogen atoms were omitted for clarity. White and yellow in (b) represent the (*P*,*P*)- and (*M*,*M*)-isomers, respectively.

The electronic absorption spectra of **1** and **2** in dichloromethane are shown in Fig. 4a. Both **1** and **2** showed broad and intense absorption bands in the range of 250–400 nm and weak HOMO → LUMO transition bands around 450 nm. The HOMO → LUMO transition band of **2** was slightly blue-shifted compared to that of **1**, which is in accordance with the TD-DFT calculations. Fig. 4b shows the emission spectra of **1** and **2** in dichloromethane at room temperature. The emission peak of **2** was observed at 547 nm, which was blue-shifted by 1246 cm^{-1} compared to that of **1** (587 nm). The emission quantum yields of **1** and **2** under the measurement conditions were 3.3% and 0.3%, respectively, showing a drastic decrease in the fluorescence quantum yield by replacing oxygen with sulfur.

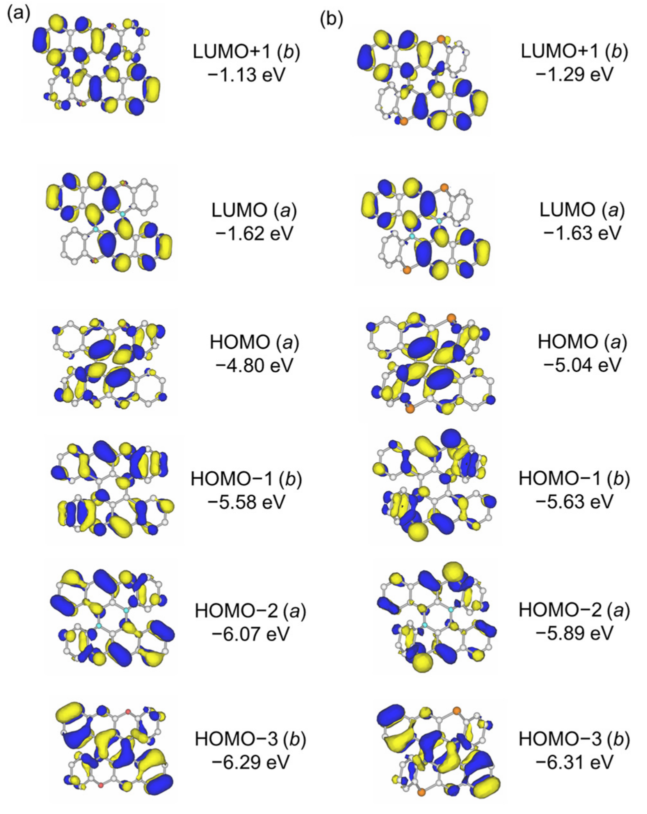

Fig. 3 Frontier Kohn-Sham molecular orbitals of (a) **1** and (b) **2** calculated at the B3LYP-GD3BJ/6-311G(2d,p) level.

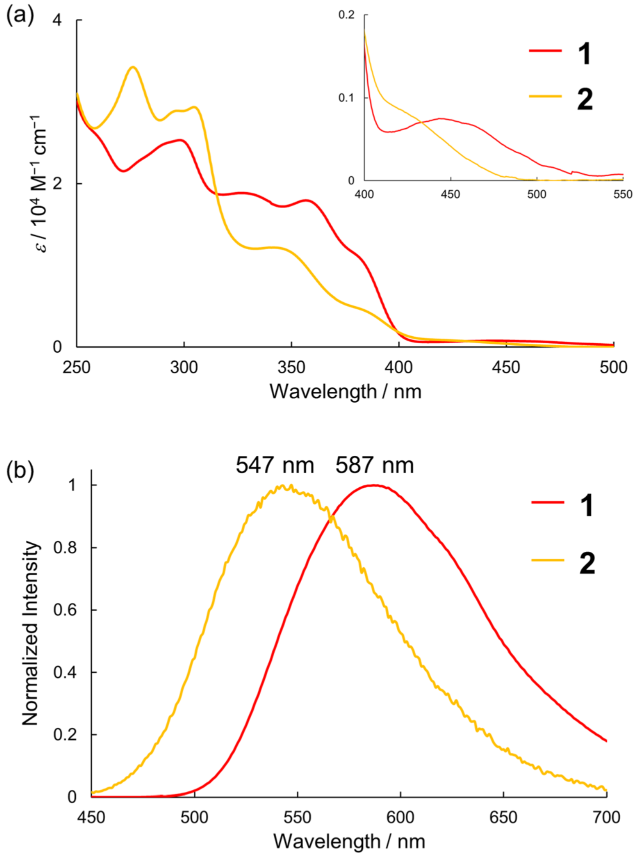

Fig. 4 (a) Absorption and (b) emission spectra (λ_{ex} = 365 nm) of **1** and **2** in dichloromethane at room temperature.

We measured the emission spectra of **1** and **2** upon lowering the temperature in 2-methyltetrahydrofuran (2-MeTHF, melting point (T_m) = 137 K, glass transition temperature (T_g) = 91 K). Fig. 5a shows the changes in the emission spectra of **1** from 293 K to 78 K. Upon cooling from 293 K to 133 K, the emission band around 600 nm gradually increased without a significant peak shift. Upon further cooling, the emission peak slightly shifted to the higher-energy region and reached 570 nm at 93 K. The observed hypsochromic shift below T_m (137 K) is due to the increase in the solvent relaxation time of supercooled liquid 2-MeTHF.[27,28] At near liquid-nitrogen temperature, new emission peaks appeared at 621 nm and 682 nm. The decay curves of the emission intensity at 621 nm and 682 nm contained a long-lived component with a lifetime of 0.17 s (Fig. S8 and S9, ESI†), indicating these emissions are phosphorescence. Due to the long-lived phosphorescence, the solution of **1** in liquid nitrogen showed a red afterglow (Fig. 5a and Movie S1, ESI†). The emission quantum yield of **1** in liquid nitrogen was 14%. The 2-MeTHF solution of **2** emitted very weak emission around 500–550 nm from 293 K to 98 K (Fig. 5b and Fig. S10, ESI†). However, upon cooling below 93 K, an emission band with shoulder peaks rose sharply in the wavelength range longer than 550 nm. The emission intensity at 78 K was more than 100 times larger than that at 293 K. The emission quantum yield of **2** in liquid nitrogen reached as high as 30%. The 2-MeTHF solution of **2** emitted an orange color at liquid-nitrogen temperature under irradiation with UV light, and an orange afterglow was observed after the UV was turned off (Fig. 5b and Movie S1, ESI†). The emission lifetime of **2** (594 nm) at 78 K was 0.22 s (Fig. S12, ESI†). Therefore, the emission observed at low temperature was attributed to phosphorescence.

The powder samples of **1** and **2** did not exhibit phosphorescence under air or vacuum, even at liquid nitrogen temperature, suggesting that aggregation leads to quenching of phosphorescence (Fig. S13 and S14, ESI†). Then, we dispersed **1** and **2** in a host material to prevent intermolecular interactions and tested their emission behaviors. The films of **1** and **2** doped in PMMA (**1**@PMMA and **2**@PMMA) did not show RTP under air. On the other hand, **1** and **2** doped into β-estradiol, which has been reported to be a good host material for RTP by Hirata *et al.*, exhibited RTP under air.[17–21,29] Under the irradiation of 365 nm light, the doped films of **1** and **2** in β-estradiol (**1**@β-estradiol and **2**@β-estradiol) exhibited yellow and orange luminescence, respectively. After the irradiation was turned off, the doped films emitted red and orange afterglows detectable with the naked eye at room temperature, respectively (Movies S2 and S3, ESI†). The results indicate that the high rigidity and oxygen barrier property of β-estradiol can sufficiently suppress the quenching of the excited triplet states of **1** and **2**. Fig. 6a and b show the emission spectra of **1**@β-estradiol and **2**@β-estradiol or PMMA measured at room temperature.

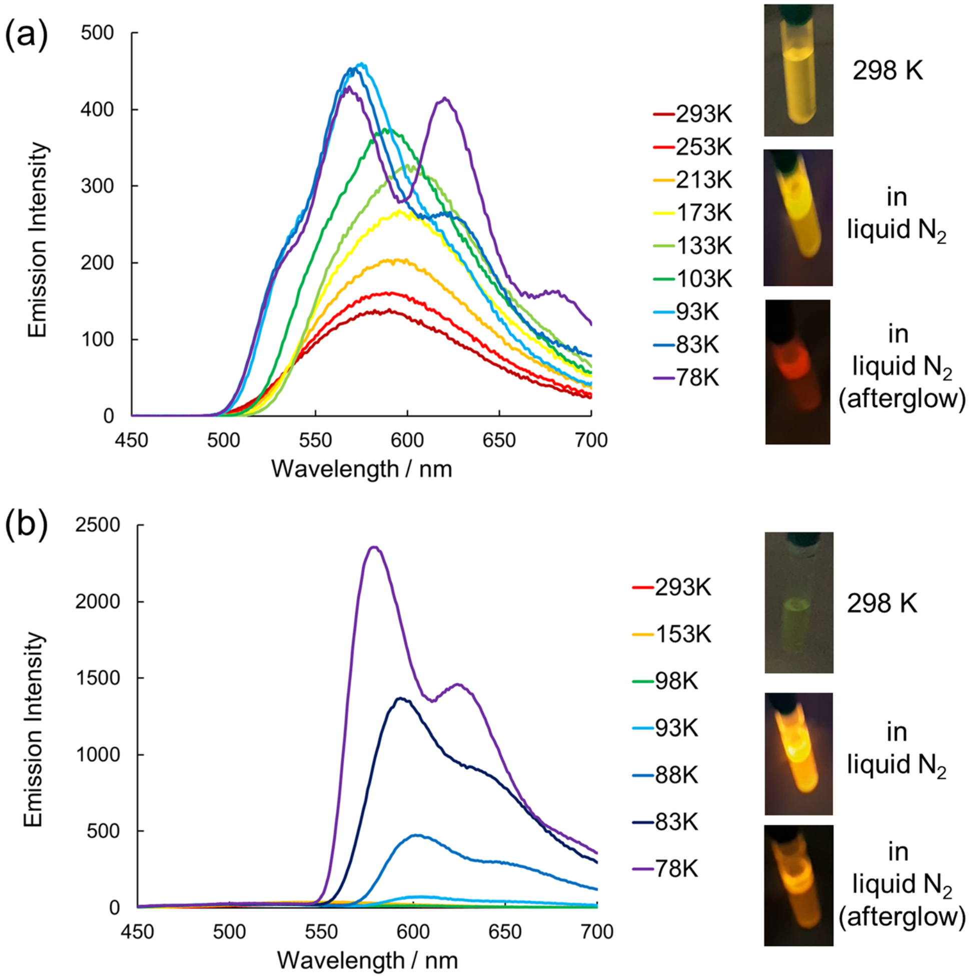

Fig. 5 Temperature dependence of the emission spectra (λ_{ex} = 365 nm) of (a) **1** and (b) **2** in 2-MeTHF (1×10^{-5} M) and photographs of the solutions at 298 K and 77 K (in liquid N_2) under irradiation with UV light at 365 nm.

Whereas **1**@PMMA showed an emission band at 566 nm attributable to fluorescence, the **1**@β-estradiol showed an emission band at 566 nm and a shoulder peak at 621 nm attributable to phosphorescence, as in the frozen solution of 2-MeTHF. The lifetime of the emission intensity at 621 nm of **1**@β-estradiol was 0.13 s at room temperature (Fig. S15, ESI†). On the other hand, the lifetime of the emission at the shorter wavelength region (500 nm) was 38 ns, indicating that the shorter-wavelength band is fluorescence (Fig. S16, ESI†). The emission quantum yield of **1**@β-estradiol was 16%, which increased from that measured in dichloromethane at room temperature (3.3%). **2**@PMMA showed a weak emission at 534 nm, attributable to fluorescence at room temperature. On the other hand, **2**@β-estradiol showed a weak band around 540 nm and an intense band at 594 nm at room temperature (Fig. 6b). The lifetimes at 480 nm and 594 nm were 1.5 ns and 0.16 s, respectively, indicating that the weaker band is fluorescence and the intense band is phosphorescence (Fig. S17 and S18, ESI†). The total emission quantum yield of **2**@β-estradiol was 34%, which was more than a hundredfold than that measured in dichloromethane at room temperature (0.3%). The emission spectrum of **2**@β-estradiol was well fitted with four Gaussian functions: one attributed to fluorescence and the other to phosphorescence (Fig. S19, ESI†). The fitting indicated that phosphorescence accounts for 87% of the total emission intensity, and the phosphorescence quantum yield (Φ_p) was estimated to be 30%. Although **1**@PMMA and **2**@PMMA did not show RTP under air, **2**@PMMA started to show RTP by removing air around the film (Fig. S20, ESI†). This result indicates the superior oxygen barrier property of β-estradiol than PMMA.

A long lifetime and high quantum efficiency are desirable properties for phosphorescence-emitting materials, but it is generally difficult to achieve both in principle.[25] Interestingly, **2** showed more intense phosphorescence and a longer phosphorescence lifetime than **1**. Therefore, we may derive hints for design guidelines for high-performance phosphorescence emitters by investigating why **2** combines a higher quantum yield and a longer lifetime than **1**. We examined the difference in the deexcitation processes between **1** and **2** by theoretical calculations. Fig. 7 shows the energy diagrams of the lower singlet and triplet excited states of **1** and **2**. The S_1 states of **1** and **2** at the equilibrium geometries of the S_1 states (S_1@S_1) are 2.212 eV

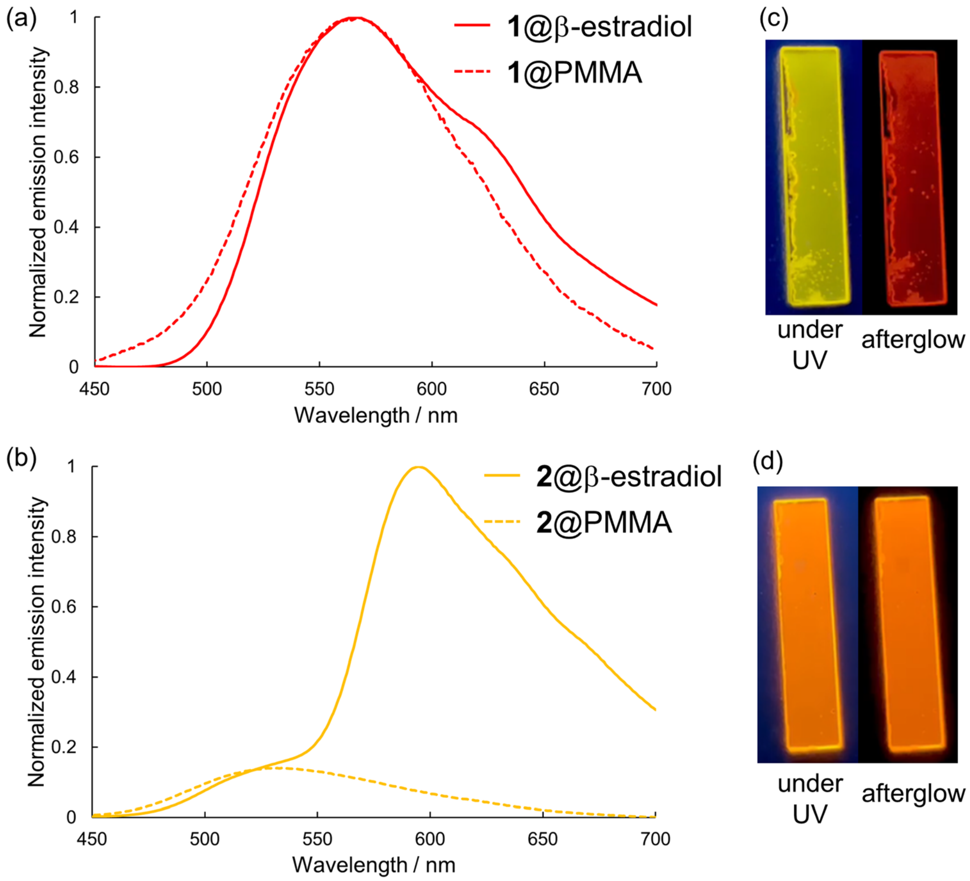

Fig. 6 (a) and (b) Emission spectra (λ_{ex} = 365 nm) of (a) **1** and (b) **2** doped in β-estradiol and PMMA measured at room temperature. (c) and (d) Photographs of the films of **1** and **2** doped in β-estradiol taken under irradiation with UV light at 365 nm and just after turning it off at room temperature.

and 2.429 eV above the S_0 states at the equilibrium geometries of the S_0 states ($S_0@S_0$). The T_1 states of **1** and **2** at the equilibrium geometries of the S_1 states ($T_1@S_1$) are lower than those of the $S_1@S_1$ states by 0.451 eV and 0.457 eV, respectively. Therefore, the $S_1 \rightarrow T_1$ intersystem crossing (ISC) rates will be small due to the large energy gaps. For **1**, the $T_2@S_1$ state is 0.176 eV above the $S_1@S_1$ state, and the $S_1 \rightarrow T_2$ ISC is energetically uphill. However, for **2**, the $T_2@S_1$ state is only 0.004 eV below the $S_1@S_1$ state, and the energy matching of the S_1 and T_2 states is thought to facilitate the $S_1 \rightarrow T_2$ ISC. We also calculated the spin-orbit coupling constants (SOCCs) $\langle S_m|\hat{H}_{SOC}|T_n\rangle$ for each ISC process within the effective nuclear charge approximation[30] by using our in-house code. Each SOCC value in Fig. 7 indicates the root sum square of SOCCs between S_m and $T_{n,\,i}$ (i = +1, 0, −1). The SOCC value for the $S_1 \rightarrow T_2$ ISC of **2** is calculated to be 2.83 cm^{-1}, which is more than twice that

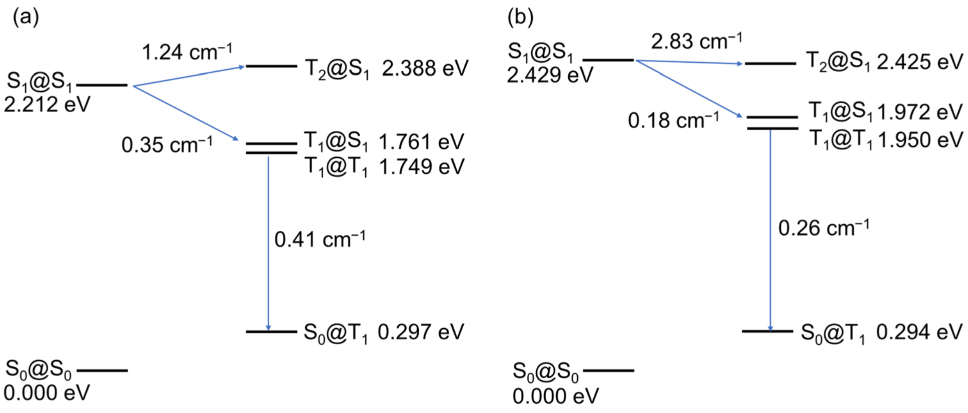

Fig. 7 Energy levels of the ground and excited states and the spin-orbit coupling constants among them for (a) **1** and (b) **2** calculated at the B3LYP-GD3BJ/6-311G(2d,p) level.

of **1** (1.24 cm^{-1}). Both the proximity of the S_1 and T_2 states and the larger SOCC for the $S_1 \rightarrow T_2$ ISC explain the efficient phosphorescence of **2**. Interestingly, **1** has the larger SOCCs than **2**, except for the $S_1 \rightarrow T_2$ process. The SOCCs for $T_1 \rightarrow S_0$, which are relevant to the phosphorescence lifetime, are 0.41 cm^{-1} for **1** and 0.26 cm^{-1} for **2**, and this result is consistent with the longer phosphorescence lifetime of **2** than **1**. This result can be understood from the electronic configurations of each excited state. The electronic configurations of the S_1 and T_1 states predominantly correspond to the one-electron excitation from HOMO to LUMO in both **1** and **2** (Table S3 and S4, ESI†). Because HOMO and LUMO of **2** have little MO coefficients on the sulfur atoms, the heavy atom effect of the sulfur substitution could be negligibly small for the $S_1 \rightarrow T_1$ and $T_1 \rightarrow S_0$ ISC processes. On the other hand, the T_2 state contains certain contributions of excitations from HOMO−1 (21.2%) and HOMO−2 (7.1%), which have significant MO coefficients on sulfur atoms, presumably resulting in the larger SOCC value for the $S_1 \rightarrow T_2$ ISC of **2**.

The enantiomers of **2** were successfully separated using HPLC with a chiral silica gel column (Fig. S26, ESI†). The CD spectra of the separated fractions of **2** were mirror images, and the faster-eluting enantiomer showed the first negative Cotton effect, similar to the case of **1** (Fig. 8a). The TD-DFT calculations reproduced the observed CD spectra well, indicating that the faster-eluting enantiomer is (*P*,*P*)-**2** (Fig. 8b). The experimental g_{CD} value of (*P*,*P*)-**2** (at 440 nm) was -2.0×10^{-2}. No racemization of the enantiomers of **2** was detected after heating in toluene at 100 °C for 13 hours. The racemization barrier of **2** was calculated to be 211.8 kJ mol^{-1} by DFT calculations, which was much higher than the calculated value of **1** (147.8 kJ mol^{-1}), indicating the extremely high resistance to racemization of **2** (Fig. S23, ESI†).

Encouraged by the success of the optical resolution and the phosphorescence properties of **2**, we measured CPL of **2** in a β-estradiol matrix at room temperature. The films of (*P*,*P*)- and (*M*,*M*)-**2** doped in β-estradiol showed clear CPL spectra of mirror images (Fig. 9a). (*P*,*P*)-**2** showed the negative sign of CPL, which is in accordance with the first negative Cotton effect in CD measured in dichloromethane and in β-estradiol (Fig. S27, ESI†). The shapes of the CPL spectra completely matched the emission spectra measured simultaneously in the apparatus (Fig. S28, ESI†). The intense CPL band around 600 nm was assigned to circularly polarized phosphorescence (CPP), judging from the lifetime of 0.16 s at 594 nm. The $|g_{CPL}|$ values at 600 nm were 5×10^{-3}. We could observe weaker shoulder bands around 500 nm, originating from fluorescence. The plots of the wavelength dependence of $|g_{CPL}|$ clearly indicate the different origins of the emissions around 500 nm and 600 nm (Fig. 9b). The $|g_{CPL}|$ values at 500 nm were 1.7×10^{-2}.

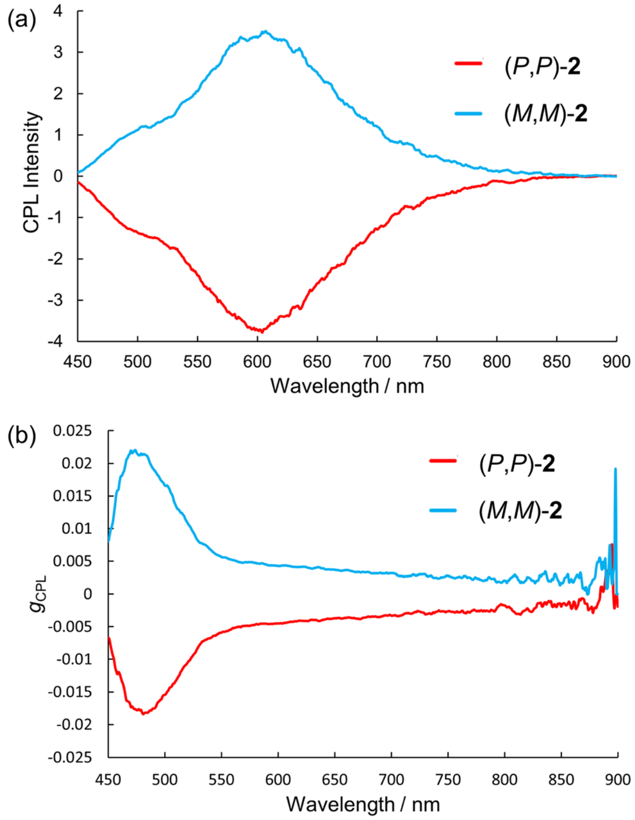

Fig. 9 (a) CPL spectra and (b) g_{CPL} of **2** doped in β-estradiol measured at room temperature (λ_{ex} = 365 nm).

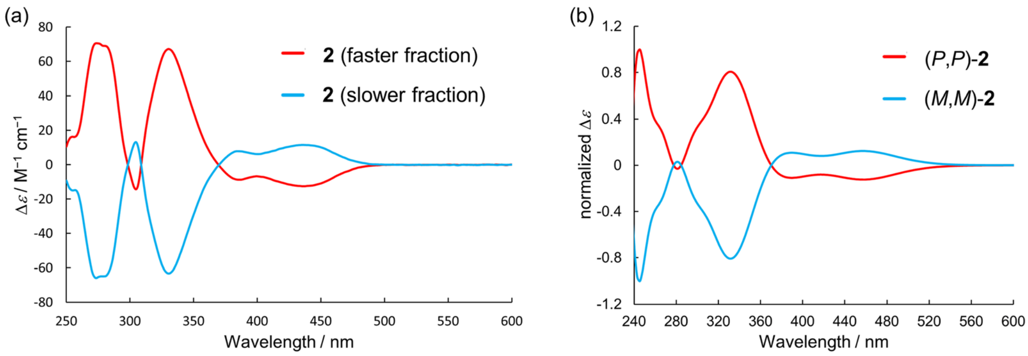

Fig. 8 (a) CD spectra of **2** measured in dichloromethane at room temperature and (b) simulated CD spectra of **2** at the B3LYP-GD3BJ/6-311G(2d,p) level.

Next, we measured the CPL spectra of the enantiomers of **2** in 2-MeTHF at 83 K with a cryostat set in the CPL spectrometer. Similar to the CPL spectra measured in β-estradiol matrix at room temperature, intense phosphorescence bands around 600 nm and weaker fluorescence bands around 500 nm were observed (Fig. S29, ESI†). The $|g_{\mathrm{CPL}}|$ values at 500 and 600 nm were 1.5×10^{-2} and 5×10^{-3}, respectively. The similarity of the spectra measured in β-estradiol and in 2-MeTHF confirmed that **2** is well dispersed in a β-estradiol matrix and the observed CPL stems from the non-aggregated molecules. The $|g_{\mathrm{CPL}}|$ value of fluorescence of **2** ($> 10^{-2}$) is comparable to that of **1** in solution and relatively large for small π-conjugated molecules. The larger $|g_{\mathrm{CPL}}|$ value of fluorescence is understood from the small oscillator strength for the S_1–S_0 transition and the parallel alignment of the transition electronic/magnetic dipole moments in **2** with a C_2 symmetrical geometry (Table S5 and Fig. S25, ESI†).[7] Over the last few years, some organic molecules exhibiting long-lived CPP at room temperature have been reported.[18,31–38] However, small molecules that emit long-lived CPP from a single-molecule state are still rare. To the best of our knowledge, this is the first example of a purely organic (not coordinating to metal ions) helicene that exhibits long-lived CPP from a non-aggregated state at room temperature. Considering the long-lived CPP properties ($|g_{\mathrm{CPL}}|$ value of phosphorescence of 5×10^{-3}, lifetime of 0.16 s, and Φ_{p} of 30%) and ease of synthesis, **2** and related analogs appear promising as functional chiroptical materials.

Conclusion

In conclusion, we have synthesized a novel double N,S-hetero[5]helicene (**2**) composed of two benzo[*b*]phenothiazine (**BPT**) units and compared its structure and electronic properties with the *N*,*O*-analogue (**1**). **2** was readily obtained by a tandem oxidative coupling of **BPT**. X-ray crystal analysis revealed that the substitution of *O* with *S* significantly increased the helical pitch of the helicene moieties of **2**. As a result, the packing structure of **2** completely changed from the homochiral columnar stacks observed in **1** to columnar stacks composed of alternating enantiomers. The substitution of *O* with *S* largely affected the photophysical properties. **2** emitted strong phosphorescence in solution at near liquid nitrogen temperature and even at room temperature by doped in a β-estradiol matrix. Theoretical calculations indicated that the singlet excited state of **2** undergoes faster intersystem crossing than **1** *via* the $S_1 \rightarrow T_2$ pathway because of the energetic proximity of S_1 and T_2 and the large SOCC for the $S_1 \rightarrow T_2$ ISC. At the same time, **2** exhibited the longer phosphorescence lifetime than **1** because of the smaller SOCC for the $T_1 \rightarrow S_0$ ISC. We have demonstrated that **2** exhibits dual circularly polarized luminescence originating from fluorescence ($|g_{\mathrm{CPL}}| > 10^{-2}$) and room-temperature phosphorescence ($|g_{\mathrm{CPL}}| = 5 \times 10^{-3}$). We believe that the simple molecular structure and noteworthy photophysical properties of **2** provide a useful guide for developing purely organic materials that exhibit long-lived circularly polarized phosphorescence.

Author contributions

D. S. and H. F. formulated the project. S. T. and D. S. synthesized the materials and collected NMR, MS, UV/Vis, emission and electrochemical data. D. S. collected and analyzed the single-crystal X-ray diffraction data. S. T., D. S., M. G. and K. T collected and analyzed CD, CPL and emission lifetime data. N. H. and T. S. calculated the spin-orbit coupling constants. S. T., D. S. and H. F. wrote the manuscript, and all authors contributed to revising the manuscript.

Conflicts of interest

There are no conflicts of interest to declare.

Acknowledgements

This work was supported by a Grant-in-Aid for Scientific Research (17H04874, 18K05264, 20H02726) from the Japan Society for the Promotion of Science (JSPS), a Grant-in-Aid for Transformative Research Areas (A) ''Condensed Conjugation'' (JSPS KAKENHI Grant Number JP20H05866) from MEXT, and Ogasawara Toshiaki Memorial Foundation. The theoretical calculations were performed using Research Center for Computational Science, Okazaki, Japan.

Notes and references

1 J. E. Anthony, Functionalized Acenes and Heteroacenes for Organic Electronics, *Chem. Rev.*, 2006, **106**, 5028–5048.
2 P. S. Gangadhar, G. Reddy, S. Prasanthkumar and L. Giribabu, Phenothiazine Functional Materials for Organic Optoelectronic Applications, *Phys. Chem. Chem. Phys.*, 2021, **23**, 14969–14996.
3 U. H. F. Bunz, The Larger N-heteroacenes, *Pure Appl. Chem.*, 2010, **82**, 953–968.
4 U. H. F. Bunz and J. Freudenberg, N-Heteroacenes and N-Heteroarenes as N-Nanocarbon Segments, *Acc. Chem. Res.*, 2019, **52**, 1575–1587.
5 D. Sakamaki, D. Kumano, E. Yashima and S. Seki, A Facile and Versatile Approach to Double N-Heterohelicenes: Tandem Oxidative C–N Couplings of N-Heteroacenes *via* Cruciform Dimers, *Angew. Chem., Int. Ed.*, 2015, **54**, 5404–5407.
6 D. Sakamaki, D. Kumano, E. Yashima and S. Seki, Double Hetero[4]helicene Composed of Two Phenothiazines: Synthesis, Structural Properties, and its Cationic States, *Chem. Commun.*, 2015, **51**, 17237–17240.
7 D. Sakamaki, S. Tanaka, K. Tanaka, M. Takino, M. Gon, K. Tanaka, T. Hirose, D. Hirobe, H. Yamamoto and H. Fujiwara, Double Heterohelicenes Composed of Benzo[*b*]- and Dibenzo[b,*i*]phenoxazine: A Comprehensive Comparison of Their Electronic and Chiroptical Properties, *J. Phys. Chem. Lett.*, 2021, **12**, 9283–9292.
8 D. Sakamaki, Y. Inoue, K. Shimomura, D. Taura, E. Yashima and S. Seki, Synthesis, Structure, and Electronic Properties

of a Double Hetero[4]helicene Composed of Two Phenoselenazines, *Tetrahedron Lett.*, 2023, **114**, 154294.

9 T. Mori, Chiroptical Properties of Symmetric Double, Triple, and Multiple Helicenes, *Chem. Rev.*, 2021, **121**, 2373–2412.

10 T. Katayama, S. Nakatsuka, H. Hirai, N. Yasuda, J. Kumar, T. Kawai and T. Hatakeyama, Two-Step Synthesis of Boron-Fused Double Helicenes, *J. Am. Chem. Soc.*, 2016, **138**, 5210–5213.

11 G. Longhi, E. Castiglioni, C. Villani, R. Sabia, S. Menichetti, C. Viglianisi, F. Devlin and S. Abbate, Chiroptical Properties of the Ground and Excited States of Two Thia-Bridged Triarylamine Heterohelicenes, *J. Photochem. Photobiol., A*, 2016, **331**, 138–145.

12 T. Otani, A. Tsuyuki, T. Iwachi, S. Someya, K. Tateno, H. Kawai, T. Saito, K. S. Kanyiva and T. Shibata, Facile Two-Step Synthesis of 1,10-Phenanthroline-Derived Polyaza [7]helicenes with High Fluorescence and CPL Efficiency, *Angew. Chem., Int. Ed.*, 2017, **56**, 3906–3910.

13 J. R. Brandt, F. Salerno and M. J. Fuchter, The Added Value of Small-Molecule Chirality in Technological Applications, *Nat. Rev. Chem.*, 2017, **1**, 0045.

14 H. Tanaka, M. Ikenosako, Y. Kato, M. Fujiki, Y. Inoue and T. Mori, Symmetry-based rational design for boosting chiroptical responses, *Commun. Chem.*, 2018, **1**, 38.

15 L. Zhang, I. Song, J. Ahn, M. Han, M. Linares, M. Surin, H.-J. Zhang, J. H. Oh and J. Lin, π-Extended Perylene Diimide Double-Heterohelicenes as Ambipolar Organic Semiconductors for Broadband Circularly Polarized Light Detection, *Nat. Commun.*, 2021, **12**, 142.

16 Y. Liu, Z. Ma, Z. Wang and W. Jiang, Boosting Circularly Polarized Luminescence Performance by a Double π-Helix and Heteroannulation, *J. Am. Chem. Soc.*, 2022, **144**, 11397–11404.

17 S. Hirata, K. Totani, J. Zhang, T. Yamashita, H. Kaji, S. R. Marder, T. Watanabe and C. Adachi, Efficient Persistent Room Temperature Phosphorescence in Organic Amorphous Materials under Ambient Conditions, *Adv. Funct. Mater.*, 2013, **23**, 3386–3397.

18 S. Hirata and M. Vacha, Circularly Polarized Persistent Room-Temperature Phosphorescence from Metal-Free Chiral Aromatics in Air, *J. Phys. Chem. Lett.*, 2016, **7**, 1539–1545.

19 S. Hirata, Intrinsic Analysis of Radiative and Room-Temperature Nonradiative Processes Based on Triplet State Intramolecular Vibrations of Heavy Atom-Free Conjugated Molecules toward Efficient Persistent Room-Temperature Phosphorescence, *J. Phys. Chem. Lett.*, 2018, **9**, 4251–4259.

20 S. Hirata, Molecular Physics of Persistent Room-Temperature Phosphorescence and Long-Lived Triplet Excitons, *Appl. Phys. Rev.*, 2022, **9**, 011304.

21 K. Fukasawa, Y. Sugawara, R. Tsuru, T. Yamashita and S. Hirata, Enhanced Red Persistent Room-Temperature Phosphorescence Induced by Orthogonal Structure Disruption during Electronic Relaxation, *J. Phys. Chem. Lett.*, 2022, **13**, 7788–7796.

22 Y. Shoji, Y. Ikabata, Q. Wang, D. Nemoto, A. Sakamoto, N. Tanaka, J. Seino, H. Nakai and T. Fukushima, Unveiling a New Aspect of Simple Arylboronic Esters: Long-Lived Room-Temperature Phosphorescence from Heavy-Atom-Free Molecules, *J. Am. Chem. Soc.*, 2017, **139**, 2728–2733.

23 S. Kuno, T. Kanamori, Z. Yijing, H. Ohtani and H. Yuasa, Long Persistent Phosphorescence of Crystalline Phenylboronic Acid Derivatives: Photophysics and a Mechanistic Study, *ChemPhotoChem*, 2017, **1**, 102–106.

24 H. Liu, Y. Gao, J. Cao, T. Li, Y. Wen, Y. Ge, L. Zhang, G. Pan, T. Zhou and B. Yang, Efficient Room-Temperature Phosphorescence Based on a Pure Organic Sulfur-Containing Heterocycle: Folding-Induced Spin–Orbit Coupling Enhancement, *Mater. Chem. Front.*, 2018, **2**, 1853–1858.

25 Kenry, C. Chen and B. Lin, Enhancing the Performance of Pure Organic Room-Temperature Phosphorescent Luminophores, *Nat. Commun.*, 2019, **10**, 2111.

26 H. Ma, Q. Peng, Z. An, W. Huang and Z. Shuai, Efficient and Long-Lived Room-Temperature Organic Phosphorescence: Theoretical Descriptors for Molecular Designs, *J. Am. Chem. Soc.*, 2019, **141**, 1010–1015.

27 M. Goes, M. de Groot, M. Koeberg, J. W. Verhoeven, N. R. Lokan, M. J. Shephard and M. N. Paddon-Row, Temperature Dependence of Charge-Transfer Fluorescence from Extended and U-shaped Donor-Bridge-Acceptor Systems in Glass-Forming Solvents, *J. Phys. Chem. A*, 2002, **106**, 2129–2134.

28 E. Görlach, H. Gygax, P. Lubini and U. P. Wild, Solvent Relaxation of Oxazine-4 in 2-Methyltetrahydrofuran, *Chem. Phys.*, 1995, **194**, 185.

29 S. Hirata, K. Totani, T. Yamashita, C. Adachi and M. Vacha, Large Reverse Saturable Absorption Under Weak Continuous Incoherent Light, *Nat. Mater.*, 2014, **13**, 938–946.

30 D. G. Fedorov, S. Koseki, M. W. Schmidt and M. S. Gordon, Spin-Orbit Coupling in Molecules: Chemistry Beyond the Adiabatic Approximation, *Int. Rev. Phys. Chem.*, 2003, **22**, 551–592.

31 W. Chen, Z. Tian, Y. Li, Y. Jiang, M. Liu and P. Duan, Long-Persistent Circularly Polarized Phosphorescence from Chiral Organic Ionic Crystals, *Chem. – Eur. J.*, 2018, **24**, 17444–17448.

32 X. Liang, T.-T. Liu, Z.-P. Yan, Y. Zhou, J. Su, X.-F. Luo, Z.-G. Wu, Y. Wang, Y.-X. Zheng and J.-L. Zuo, Organic Room-Temperature Phosphorescence with Strong Circularly Polarized Luminescence Based on Paracyclophanes, *Angew. Chem., Int. Ed.*, 2019, **58**, 17220–17225.

33 H. Li, H. Li, W. Wang, Y. Tao, S. Wang, Q. Yang, Y. Jiang, C. Zheng, W. Huang and R. Chen, Stimuli-Responsive Circularly Polarized Organic Ultralong Room Temperature Phosphorescence, *Angew. Chem., Int. Ed.*, 2020, **59**, 4756–4762.

34 L. Gu, W. Ye, X. Liang, A. Lv, H. Ma, M. Singh, W. Jia, Z. Shen, Y. Guo, Y. Gao, H. Chen, D. Wang, Y. Wu, J. Liu, H. Wang, Y. X. Zheng, Z. An, W. Huang and Y. Zhao, Circularly Polarized Organic Room Temperature Phosphorescence from Amorphous Copolymers, *J. Am. Chem. Soc.*, 2021, **143**, 18527–18535.

35 S. Garain, S. Sarkar, B. Chandra Garain, S. K. Pati and S. J. George, Chiral Arylene Diimide Phosphors: Circularly Polarized Ambient Phosphorescence from Bischromophoric Pyromellitic Diimides, *Angew. Chem., Int. Ed.*, 2022, **61**, e202115773.

36 H. Li, J. Gu, Z. Wang, J. Wang, F. He, P. Li, Y. Tao, H. Li, G. Xie, W. Huang, C. Zheng and R. Chen, Single-Component Color-Tunable Circularly Polarized Organic Afterglow through Chiral Clusterization, *Nat. Commun.*, 2022, **13**, 429.

37 W. Huang, C. Fu, Z. Liang, K. Zhou and Z. He, Strong Circularly-Polarized Room-Temperature Phosphorescence from a Feasibly Separable Scaffold of Bidibenzo[*b*,*d*]furan with Locked Axial Chirality. Z, *Angew. Chem., Int. Ed.*, 2022, **61**, e202202977.

38 W. Ning, H. Wang, S. Gong, C. Zhong and C. Yang, Simple Sulfone-Bridged Heterohelicene Structure Realizes Ultraviolet Narrowband Thermally Activated Delayed Fluorescence, Circularly Polarized Luminescence, and Room Temperature Phosphorescence., *Sci. China: Chem.*, 2022, **9**, 1715–1719.